Fourth order phase-field model for local *max–ent* approximants applied to crack propagation

Fatemeh Amiri[f], Daniel Millán[c], Marino Arroyo[d], Mohammad Silani[g], Timon Rabczuk[abef𝒮]

[a] *Division of Computational Mechanics, Ton Duc Thang University, Ho Chi Minh City, Vietnam.*

[b] *Faculty of Civil Engineering, Ton Duc Thang University, Ho Chi Minh City, Vietnam.*

[c] *National Scientific and Technical Research Council and Faculty of Exact and Natural Sciences, National University of Cuyo, Mendoza 5500, Argentina.*

[d] *School of Civil Engineering of Barcelona (ETSECCPB), Departament de Matemàtica Aplicada 3, Universitat Politècnica de Catalunya, Spain.*

[e] *Prof., School of Civil, Environmental and Architectural Engineering, Korea University, 136-701 Korea.*

[f] *Institute of Structural Mechanics, Bauhaus University of Weimar, 99423 Weimar, Germany.*

[g] *Department of Mechanical Engineering, Isfahan University of Technology, Isfahan 84156-83111, Iran.*

[𝒮] *Corresponding author: Timon Rabczuk, email: timon.rabczuk@tdt.edu.vn*

Abstract

We apply a fourth order phase-field model for fracture based on local maximum entropy (LME) approximants. The higher order continuity of the meshfree LME approximants allows to directly solve the fourth order phase-field equations without splitting the fourth order differential equation into two second order differential equations. We will first show that the crack surface can be captured more accurately in the fourth order model. Furthermore, less nodes are needed for the fourth order model to resolve the crack path. Finally, we demonstrate the performance of the proposed meshfree fourth order phase-field formulation for 5 representative numerical examples. Computational results will be compared to analytical solutions within linear elastic fracture mechanics and experimental data for three-dimensional crack propagation.

Keywords: Fracture, local maximum entropy, second order phase-field model, fourth order phase-field model.

Abbreviations and notations list

LME	Local Maximum Entropy
Max–ent	Maximum entropy
FEM	Finite Element Method
GFEM	Generalized Finite Element Method
IGA	Isogeometric Analysis
XIGA	eXtended Isogeometric Analysis

XFEM	eXtended Finite Element Method
PDE	Partial Differential Equation
ODE	Ordinary Differential Equation
NURBS	Non-uniform Rational Basis Spline
l_0	Length scale parameter
h	Nodal spacing
β	Thermalization parameter to control the locality of the LME basis functions
γ	$\gamma = \beta h^2$, controls degree of locality
v	Phase-field variable
$\boldsymbol{u}$	Displacement tensor
$\boldsymbol{\varepsilon}$	Strain tensor
a	The crack length
G	Energy release rate
G_c	Critical energy release rate
F_0	The elastic energy density of an undamaged body
F	The elastic energy density of a body (damaged or undamaged)
P	The external potential energy functional
E	The strain energy functional
Π	The total potential energy functional
Γ	The crack surface energy
Γ_{l_0}	The crack surface functional

1 Introduction

The modeling of fracture is of major importance in engineering applications such as aircraft fuselages, pressure vessels, automobile components, and castings. The progress in this field and the ability to prevent material failure have helped control the dangers caused by increasing technological complexity. A theoretical model for brittle fracture in solids was introduced by Griffith [28] and Irwin [34], which relates crack propagation to a critical value of the energy release rate. During the last few decades the numerical simulation of such process has gained importance and often plays a key role in design decisions [22, 59, 67]. This has been mainly motivated by the impossibility to have analytical solutions in most practical situations and the costs of obtaining meaningful and detailed information from experiments. Numerical methods, such as the finite element method have been used to model fracture with some success, but often they are unable to capture some physical properties of the phenomenon. Modeling of moving discontinuities with classical finite elements is difficult to automate because of the requirement that the mesh must conform to the surfaces of discontinuity. It also usually requires local refinement near the fracture zone, in particular near the crack tips where singularities in the stress field occur [8, 9, 10, 46].

An attractive approach to overcome these difficulties has been presented by the extended finite element method (XFEM) [16, 42] or the generalized finite element method (GFEM) [64]. These methods allow arbitrary propagating discontinuities without remeshing. One key challenge of such methods is describing the crack geometry and tracking the paths of the cracks as the fracture progresses. This becomes increasingly challenging for complex fracture patterns. In general these numerical approximations track the evolution of the fracture during the simulations but they have shown to be inefficient regarding, for example, crack branching in three dimensional applications. XIGA formulations (Extended isogeometric analysis) for frac-

ture [17, 26, 45] aim to combine the advantages of isogeometric analysis and the extended finite element method. However, they also do not resolve the issue of complex track cracking procedures. An alternative to model complex fracture are meshfree methods [1, 4, 5, 35, 49, 50, 51, 52, 53, 58, 61, 62, 66]. While those contributions also rely on the representation of the crack surface, some meshfree methods such as the Cracking Particles Method [56, 57] model fracture as a set of crack segments and therefore can capture – on cost of the accuracy in the crack kinematics – complex fracture patterns quite naturally.

Besides discrete crack models, continuous descriptions of fracture in solids have been presented. Among the most popular approaches are gradient models [23, 24, 36, 54, 55, 63] and non-local models [12, 13, 14, 15]. They introduce an intrinsic length scale and diffuse fracture over a certain width. Phase-field approaches for fracture [19] bear certain similarities to gradient models but they converge to a discrete crack model when the characteristic length tends to zero. Phase-field approaches also do not require an explicit representation of the crack surface and therefore complex crack tracking algorithms, see the recent contributions [30, 31, 32, 37, 38, 39]. The crack surface is obtained as part of the solution and it is represented by an indicator function that is equal to 0 on the crack surface and 1 away from the fracture zone. The predecessors of phase-field approaches to fracture can be traced back to 1998 in [21, 25], where the brittle crack propagation problem was regularized and recast as a minimization problem. In this model, the proposed energy functional is closely similar to the potential functional presented by Mumford and Shah [43], which has been used in image segmentation. The existence of solution to the Mumford-Shah functional minimization was proven by Ambrosio in [2]. In [3], an approximation by an elliptic functional defined on Sobolev spaces was developed, based on the theory of Γ-convergence. In the phase-field approach, a continuous field governed by a partial differential equation (PDE) is used to model the cracks and their evolution. This method naturally deals with complex crack geometries. Its main drawback is the higher computational cost of solving a coupled PDE system. In this method, the crack zone is controlled by a regularization parameter. As this regularization parameter converges to zero, the phase-field model converges to a discrete crack model.

Here we used phase-field model in combination with the local maximum-entropy (LME) method. The LME approximant schemes were developed in [11, 65] using a framework similar to meshfree methods. The support of the basis functions is introduced as a thermalization (or penalty) parameter β in the constraint equations. In [11] it was shown that for some values of β, the approximation properties of the maximum-entropy basis functions are greatly superior to those of the finite element linear functions, even when the added computational cost due to larger support is taken into account. Subsequent studies [40, 41, 47, 48], show that maximum entropy shape functions are suitable for solving a variety of problems such as linear and geometrically nonlinear thin shell analysis, compressible and nearly-incompressible elasticity and incompressible media problems. In this paper, we study the performance of a fourth order phase-field-model introduced in [18]. We show it is more efficient to use fourth order phase-field model with LME shape functions, due to the smoothness of these shape functions.

The paper is organized as follows. In Section 2 we present the general theory and motivation for the second and fourth order phase-field models. Also the continuum formulation of an elastic body with phase-field model, is presented in this section. In Section 3 Galerkin discretization formulation is presented. In Section 4, we demonstrate the capabilities of the method through some numerical examples. In this section, the convergence rate and the error of modeling of the fourth order model are compared to the second order model. Some concluding remarks are given in Section 5.

2 Governing Equations and Weak Form

2.1 Second and fourth-order phase-field model

Consider an infinite bar with cross-section Γ, occupying a region $\Omega = (-\infty, +\infty) \times \Gamma$. According to Fig. 1($a$), a crack is placed at $x = 0$. The phase-field variable $v(x) \in [0, 1]$ with

$$v(x) = \begin{cases} 0 & x = 0, \\ 1 & \text{otherwise}, \end{cases} \tag{1}$$

is introduced to describe the crack topology, where $v = 0$ indicates the crack (total damage) while $v = 1$ refers to intact state. This phase-field is discontinuous at $x = 0$ and satisfies the following conditions

$$\begin{aligned} v(0) &= 0, \\ v(\pm\infty) &= 1. \end{aligned} \tag{2}$$

A function that fulfils the criterion (1) and (2) is

$$v(x) = 1 - e^{-\frac{|x|}{2l_0}}, \tag{3}$$

when the diffusivity $l_0 \to 0$. Furthermore, as it was shown in [39], this function is the solution of a second order differential equation

$$v(x) - 4l_0^2 v'' - 1 = 0 \quad in\ \ \Omega, \tag{4}$$

subject to the essential boundary conditions given in Eq. (2). This second order differential equation leads to a second order phase-field approximation method, which computes the area of the crack by

$$\Gamma_{l_0} = \frac{1}{4l_0} \int_{-\infty}^{+\infty} (1 - v)^2 + 4l_0^2 (v')^2 dx, \tag{5}$$

with $dV = \Gamma dx$. In order to approximate this function, a C^0 basis such as the one provided by the standard finite element method (FEM) is sufficient. In meshfree methods such as LME approximants [11], the basis functions are smooth. Hence, the kink (at $x = 0$) in the phase-field might not be well-captured with these methods. Let us assume another function [18]

$$v(x) = 1 - e^{-\frac{|x|}{l_0}} \left(1 + \frac{|x|}{l_0}\right). \tag{6}$$

This function satisfies the conditions (2) and introduces smoother approximation as is demonstrated in Fig. 1(c). We find that Eq. (6) is the solution of the fourth order differential equation

$$v - 1 - 2l_0^2 v'' + l_0^4 v^{(4)} = 0 \quad in\ \ \Omega, \tag{7}$$

under the assumption that $v(0) = 0, v'(0) = 0$ and $v^\alpha(x) \to 0$ as $x \to \pm\infty$ for all $\alpha \geq 0$ [18]. The functional behind this ordinary differential equations is

$$I(v) = \frac{1}{2} \int_{-\infty}^{+\infty} (1 - v)^2 + 2l_0^2 (v')^2 + l_0^4 (v'')^2 dx. \tag{8}$$

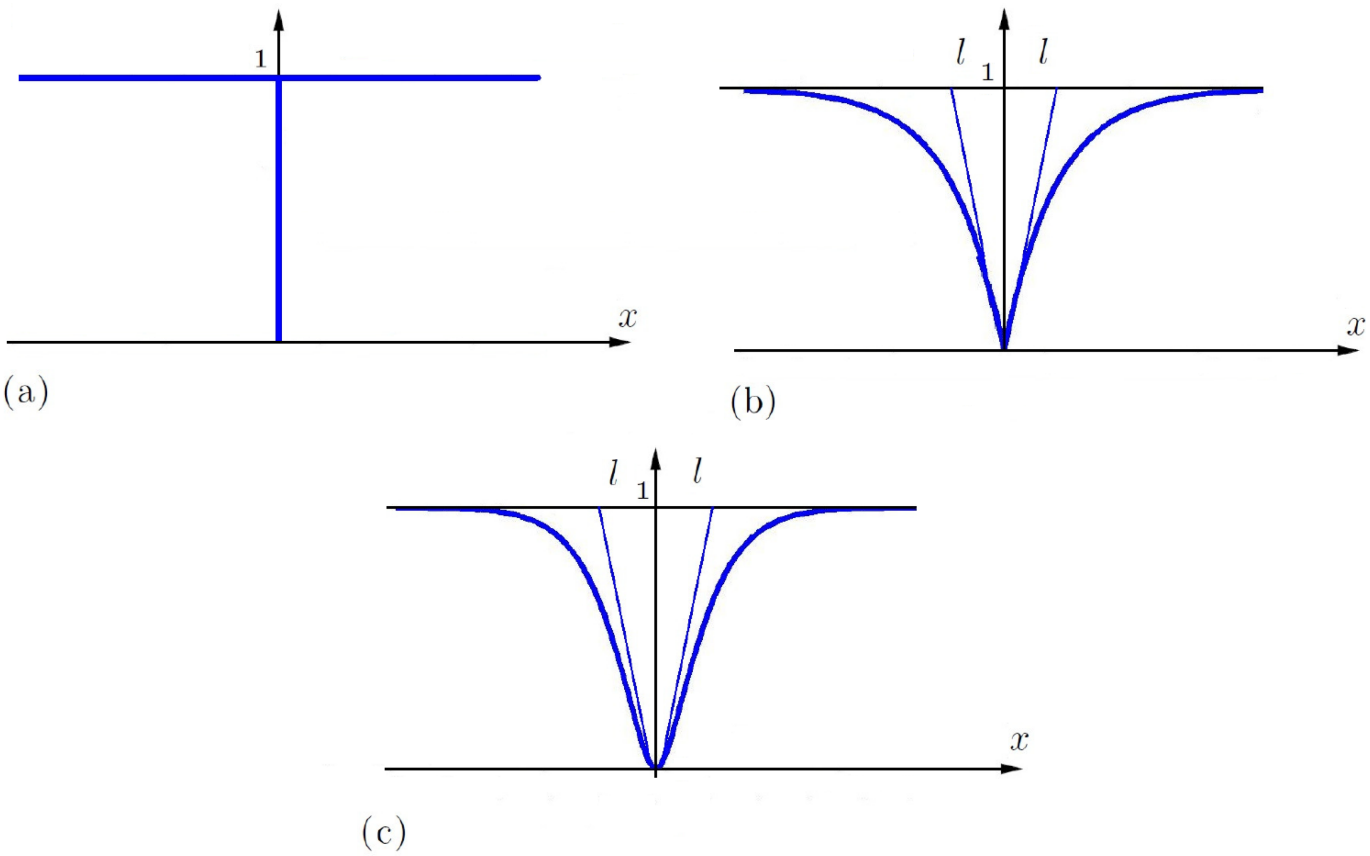

Figure 1: (a) Sharp crack at $x = 0$, (b) exponential solution of the second order phase-field model and (c) exponential solution of the fourth order phase-field model with the length scale parameter $l = 2l_0$.

The value of this functional for Eq. (6) is $2l_0\Gamma$, which gives

$$\Gamma_{l_0} = \frac{1}{4l_0}\int_{-\infty}^{+\infty}(1-v)^2 + 2l_0^2(v')^2 + l_0^4(v'')^2 dx. \tag{9}$$

As was expressed by Miehe and coworkers in [39], the functional Γ_{l_0} can be considered as the crack surface itself. Eq. (9) is the fourth order phase-field model in 1D.

Finite elements based on Lagrange polynomials are not well suited for the fourth order phase-field model which requires C^1 continuity in the phase-field. A common approach is to split the fourth-order differential equation into two second order differential equations as proposed e.g. in [6]. Due to the higher order continuity of the LME approximants, they are ideally suited to directly solve the fourth-order phase-field equations. Such an approach has been proven to be successful in isogeometric analysis (IGA) [18]. However, in contrast to IGA which requires at least a quadratic basis, only linear completeness is needed in the LME approximants.

The extension of the phase-field model to higher dimensional problems is straightforward. Assume $\Omega \subseteq R^d$, be a domain with $d \in \{1, 2, 3\}$ and $\partial\Omega \subseteq R^{d-1}$ is the boundary of this domain. The crack length can be computed by

$$\Gamma_{l_0}(v) = \int_\Omega \gamma(v, \nabla v, \Delta v) dV, \tag{10}$$

with

$$\gamma(v, \nabla v) = \frac{1}{4l_0}\left[(1-v)^2 + l_0^2 \left|\nabla v\right|^2\right], \tag{11}$$

for the second order model and

$$\gamma(v, \nabla v, \Delta v) = \frac{1}{4l_0}\left[(1-v)^2 + 2l_0^2 \left|\nabla v\right|^2 + l_0^4 \left|\Delta v\right|^2\right], \tag{12}$$

for the fourth order model.

2.2 Phase-field model for an elastic body

In [28], Griffith demonstrated that crack propagation for elastic solids is caused by the transfer of energy from external work to surface energy. He applied the first law of thermodynamics to formulate cracks in elastic solid bodies. The first law of thermodynamics states that the change of total energy is equal to the sum of the change of work done by the external forces and the change of heat content per unit time. Since, the loads are applied in a quasi static behavior in this work, the change of heat and the kinetic energy are zero. The change of the total energy for this case, can be written as

$$\frac{\partial}{\partial a}(E + \Gamma) = \frac{\partial P}{\partial a} \tag{13}$$

Here E is the total internal strain energy, Γ the surface energy, a indicates the crack length and P the external work. Therefore, following Griffith model for brittle material, we define

$$G = \frac{\partial \Gamma}{\partial a} = \frac{\partial P}{\partial a} - \frac{\partial E}{\partial a}, \tag{14}$$

where G is the energy release rate or the crack driving force. The material parameter G_c is the critical energy release rate or the surface energy density. The crack propagates when G gets G_c, where the crack surface energy is approximated by

$$\Gamma \approx G_c \Gamma_{l_0},$$

Γ_{l_0} is the crack surface functional defined in Eq. (10).

For a linear elastic isotropic solid, the strain energy is expressed as

$$E = \int_\Omega F(\boldsymbol{\varepsilon}(\boldsymbol{u}), v) dV, \tag{15}$$

We assume traction free conditions on the crack faces. In order to satisfy this condition, the elastic energy density of an undamaged solid, F_0, is multiplied by the jump set function $g(v)$ yielding

$$F(\boldsymbol{\varepsilon}(\boldsymbol{u}), v) = g(v) F_0(\boldsymbol{\varepsilon}(\boldsymbol{u})), \tag{16}$$

where $F_0(\boldsymbol{\varepsilon}(\boldsymbol{u})) = \frac{1}{2}\boldsymbol{\varepsilon}(\boldsymbol{u}) \colon \boldsymbol{C} \colon \boldsymbol{\varepsilon}(\boldsymbol{u})$. Here $\boldsymbol{C}$ is the elasticity tensor and $\boldsymbol{\varepsilon}(\boldsymbol{u}) = \boldsymbol{D}\boldsymbol{u}$ with

$$\boldsymbol{D} = \begin{pmatrix} \frac{\partial}{\partial x_1} & 0 & 0 \\ 0 & \frac{\partial}{\partial x_2} & 0 \\ 0 & 0 & \frac{\partial}{\partial x_3} \\ \frac{\partial}{\partial x_2} & \frac{\partial}{\partial x_1} & 0 \\ 0 & \frac{\partial}{\partial x_3} & \frac{\partial}{\partial x_2} \\ \frac{\partial}{\partial x_3} & 0 & \frac{\partial}{\partial x_1} \end{pmatrix}.$$

The function $g(v)$ is assumed to satisfy the following conditions,

$$g(0) = 0, g(1) = 1, g'(0) = 0, \tag{17}$$

$$\forall v_1, v_2 \in [0,1], \;\; if \;\; v_1 \leq v_2 \Rightarrow g(v_1) \leq g(v_2). \tag{18}$$

The first and second condition in Eq. (17), are the limits for the fully damage and undamaged case. The third condition states that when $v \to 0$, the energy converges to a finite value. A simple function that meets these requirements, is

$$g(v) = v^2 + k \tag{19}$$

The parameter $k \ll 1$ is introduced in the case of the second order phase-field model to avoid the singularity of disappearing internal energy density when the phase-field parameter is zero. However, in the case of the fourth order phase-field model, it is not necessary [18]. Consider the external potential energy functional

$$P(\boldsymbol{u}) = \int_\Omega \boldsymbol{b}(x) \cdot \boldsymbol{u} dV + \int_{\Gamma_t} \boldsymbol{t}_N(x) \cdot \boldsymbol{u} d\Gamma_t, \tag{20}$$

where $\boldsymbol{b}(x)$ is body force and $\boldsymbol{t}_N(x)$ are the tractions. The total potential energy functional is introduced as

$$\Pi(\boldsymbol{u}, v) = E(\boldsymbol{u}, v) + G_c \Gamma_{l_0} - P(\boldsymbol{u}). \tag{21}$$

Since the variations $\delta\boldsymbol{u}$ and δv are independent, the first variation of the functional, $\Pi(\boldsymbol{u}, v)$, leads to two coupled equations

$$\delta\Pi(\boldsymbol{u}, v, \delta\boldsymbol{u}) = \delta_{\boldsymbol{u}} E(\boldsymbol{u}, v) - \delta_{\boldsymbol{u}} P(\boldsymbol{u}) = 0, \tag{22}$$

$$\delta\Pi(\boldsymbol{u}, v, \delta\boldsymbol{u}) = \int_\Omega [v^2 + k] \delta_{\boldsymbol{u}} F_0(\boldsymbol{\varepsilon}(\boldsymbol{u})) dV - \left[\int_\Omega \boldsymbol{b}(x) \cdot \delta\boldsymbol{u} dV + \int_{\Gamma_t} \boldsymbol{t}_N(x) \cdot \delta\boldsymbol{u} d\Gamma_t \right] = 0. \tag{23}$$

$$\delta\Pi(\boldsymbol{u}, v, \delta v) = \delta_v E(\boldsymbol{u}, v) + G_c \delta_v \Gamma_{l_0} = 0 \tag{24}$$

For the second order phase-field model, we obtain

$$\delta\Pi_{2^{nd}}(\boldsymbol{u}, v, \delta v) = \int_\Omega \left\{ 2v\delta v F_0(\boldsymbol{\varepsilon}(\boldsymbol{u})) + \frac{G_c}{2l_0} [-\delta v + v\delta v + 4l_0^2 \nabla v \cdot \nabla(\delta v)] \right\} dV, \tag{25}$$

and for the fourth order phase-field model

$$\delta\Pi_{4^{th}}(\boldsymbol{u}, v, \delta v) = \int_\Omega \left\{ 2v\delta v F_0(\boldsymbol{\varepsilon}(\boldsymbol{u})) - \frac{G_c}{2l_0} \delta v + \frac{G_c}{2l_0} [v\delta v + 2l_0^2 \nabla v \cdot \nabla(\delta v) + l_0^4 \Delta v \cdot \Delta(\delta v)] \right\} dV. \tag{26}$$

The decoupled equations can be solved by a staggered scheme that is more robust as demonstrated e.g. in [31].

3 Discretization with LME approximants

We consider now the discrete equilibrium equations of (22) and (24), and approximate $\boldsymbol{u}$ and v as follows

$$\boldsymbol{u}(\boldsymbol{x}) = \sum_a p_a \boldsymbol{u}_a, \tag{27}$$

$$v(\boldsymbol{x}) = \sum_a p_a v_a, \tag{28}$$

where p_a are LME basis functions and $\boldsymbol{u}_a$ and v_a are nodal displacement and phase-field parameter. Virtual displacements and virtual phase-field parameters are represented likewise. The LME basis functions are non-negative and satisfy the zeroth-order and first-order consistency conditions

$$p_a(\boldsymbol{x}) \geq 0, \tag{29}$$

$$\sum_{a=1}^{N} p_a(\boldsymbol{x}) = 1, \tag{30}$$

$$\sum_{a=1}^{N} p_a(\boldsymbol{x}) \boldsymbol{x}_a = \boldsymbol{x}. \tag{31}$$

In the last equation, the vector $\boldsymbol{x}_a$ identifies the positions of the nodes associated with each basis function. The maximum entropy basis functions can be designed to satisfy quadratic consistency as well [60], but we do not consider these approximations here. The local maximum entropy basis functions are written in the form:

$$p_a(\boldsymbol{x}) = \frac{1}{Z(\boldsymbol{x}, \lambda^*(\boldsymbol{x}))} \exp[-\beta_a \left|\boldsymbol{x} - \boldsymbol{x}_a\right|^2 + \lambda^*(\boldsymbol{x}) \cdot (\boldsymbol{x} - \boldsymbol{x}_a)],$$

where

$$Z(\boldsymbol{x}, \lambda) = \sum_{b=1}^{N} \exp[-\beta_b \left|\boldsymbol{x} - \boldsymbol{x}_b\right|^2 + \lambda \cdot (\boldsymbol{x} - \boldsymbol{x}_b)],$$

is a function associated with a set of nodes $X = \{\boldsymbol{x}_a\}_{a=1,\ldots,N}$ and $\lambda^*(\boldsymbol{x})$ is defined by

$$\lambda^*(\boldsymbol{x}) = \arg \min_{\lambda \in \mathbb{R}^d} \log\ Z(\boldsymbol{x}, \lambda).$$

The LME basis functions are smooth (C^∞) [11]. In this paper we choose $\beta = \frac{\gamma}{h^2}$, where h is a measure of the nodal spacing and γ is constant over the domain. In this case the basis functions are smooth and their degree of locality is controlled by the parameter γ. As it was studied in [11, 4], the optimal support size of the basis functions or γ value is problem dependent. It is also shown that choosing $\gamma \geq 4.8$ gives almost the same results as standard finite element method. While decreasing γ gives smoother LME basis functions. The LME basis functions satisfy a weak Kronecker delta property at the boundary of the convex hull of the nodes. Therefore, the basis functions that correspond to interior nodes vanish on the boundary.

Replacing the variation of the strain energy density into the Eq. (23), we obtain

$$\delta\Pi[\boldsymbol{u}, v, \delta\boldsymbol{u}] = \int_\Omega [v^2 + k]\{\boldsymbol{D}(\delta\boldsymbol{u}) : \boldsymbol{C} : \boldsymbol{D}\boldsymbol{u}\} dV - \left[\int_\Omega \boldsymbol{b}(x) \cdot \delta\boldsymbol{u} dV + \int_{\Gamma_t} \boldsymbol{t}_N(x) \cdot \delta\boldsymbol{u} d\Gamma_t\right] = 0. \tag{32}$$

Approximating $\boldsymbol{u}$ and $\delta\boldsymbol{u}$ with (27) and a simple calculation yields the Galerkin stiffness matrix. The interaction between nodes a and b for displacement field is given by

$$\boldsymbol{K}_{\boldsymbol{u}}^{ab} = \int_{\Omega} [v^2 + k]\boldsymbol{B}^a \boldsymbol{C}\boldsymbol{B}^{bT} dV, \tag{33}$$

where

$$\boldsymbol{B}^a = \boldsymbol{D}p_a.$$

The force contribution of the a-th node is

$$\boldsymbol{f}_{\boldsymbol{u}}^a = \int_{\Omega} \boldsymbol{b}p_a dV + \int_{\Gamma_t} \boldsymbol{t}_N p_a d\Gamma_t. \tag{34}$$

Finally, the phase-field stiffness matrix for the second and fourth order are

$$\boldsymbol{K}_v^{ab} = \int_{\Omega} \left\{ [2F_0(\boldsymbol{\varepsilon}(\boldsymbol{u})) + \frac{G_c}{2l_0}]p_a p_b + 2G_c l_0 \nabla p_a \nabla p_b \right\} dV \tag{35}$$

$$\boldsymbol{K}_v^{ab} = \int_{\Omega} \left\{ [2F_0(\boldsymbol{\varepsilon}(\boldsymbol{u})) + \frac{G_c}{2l_0}]p_a p_b + \frac{G_c}{l_0}[l_0^2 \nabla p_a \nabla p_b + \frac{l_0^4}{2}\Delta p_a \Delta p_b] \right\} dV \tag{36}$$

and the right hand side for phase-field is

$$\boldsymbol{f}_v^a = \int_{\Omega} \frac{G_c}{2l_0} p_a dV. \tag{37}$$

In this model, cracks can propagate, branch and merge but can not reverse, whereas this feature is reached by imposing $v^i \leq v^{i-1}$, such that v^{i-1} and v^i are the phase-field parameters at step $i-1$ and i [20].

4 Numerical Examples

4.1 Solution of the pure phase-field equation

4.1.1 One-dimensional problem

First, we determine how well the proposed second and fourth order models approximate the "crack topology". For simplicity, we start with the 1D model explained in Section 2. We set the Dirichlet boundary condition $v = 0$, for $x = 0$. We compute the error in the L^2 norm and H^1 semi-norm for the second order model by considering Eq. (3) as exact solutions and $L = 1$. As it is obvious from Fig. 2, the best results are obtained for $\gamma = 5.8$. The rate of convergence in the L^2 norm in this case is about 1.7, while the rate of convergence for $\gamma < 2.8$ is about 1.0. The convergence rate in the H^1 semi-norm is optimal, i.e. equal 1, with $\gamma = 5.8$ but sub-optimal (order 0.4) for $\gamma \leq 2.8$. This is due to the smooth basis functions used to approximate a non-smooth solution. For $\gamma = 5.8$, the LME basis functions are much sharper and rigorously approach the C^0 finite element shape functions for $\gamma \to \infty$.

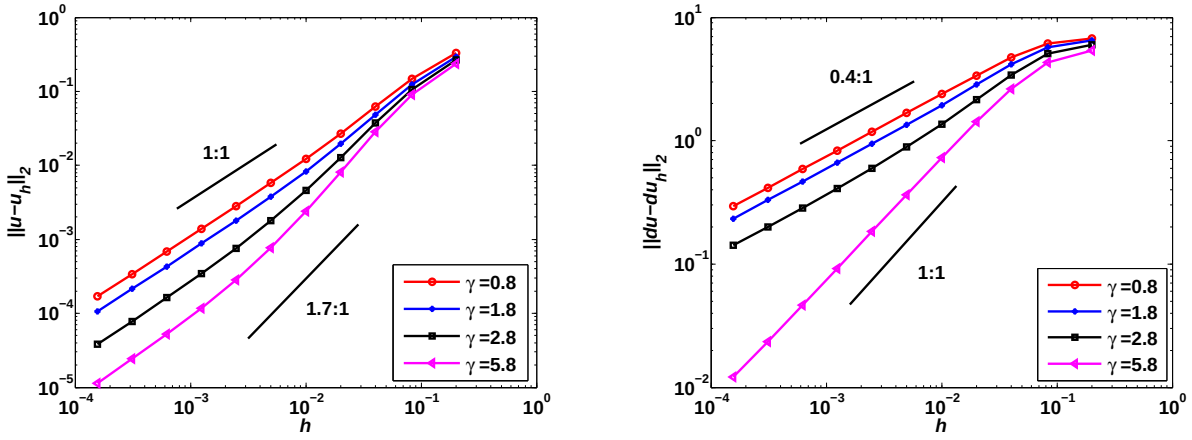

(a) (b)

Figure 2: L2 norm and Semi-norm H^1 errors of the solution of the second order ODE in Eq. (4), as a function of nodal spacing, h, with $l_0 = 0.025$ and different values of γ.

For the fourth order phase-field model, we compute the error in the L^2 norm, H^1 semi-norm and H^2 semi-norm. For the LME basis functions, the best results are obtained for $\gamma = 0.6$, and the rate of convergence of the L^2 norm error is about 4, which is super convergent. As can be seen from Fig. 3a, for values of $\gamma \geq 0.8$ no convergence in the L^2 norm is obtained. Note that, in contrast to the at least quadratic NURBS–formulation, we employ basis functions that possess up to first-order reproducing conditions. Strictly speaking, to solve the fourth order PDE, functions that reproduce quadratic polynomials are required [33], and hence we should use quadratic max-ent approximants. However, it has already been shown that, in practice, linear max-ent approximants with low value of gamma effectively behave like quadratic consistent approximants, and the convergence rate in fourth order PDE (thin shells and phase-field models of membranes) is only degraded for very fine meshes and very small errors [5, 41]. Figs. 3 and 4 agree with this behavior, in that convergence is degraded only for high values of γ and for very fine grids.

Figs. 3b and 4 illustrate the error in the H^1 and H^2 semi-norm. The rate of convergence for $\gamma = 0.6$ is around 3 and 2, respectively.

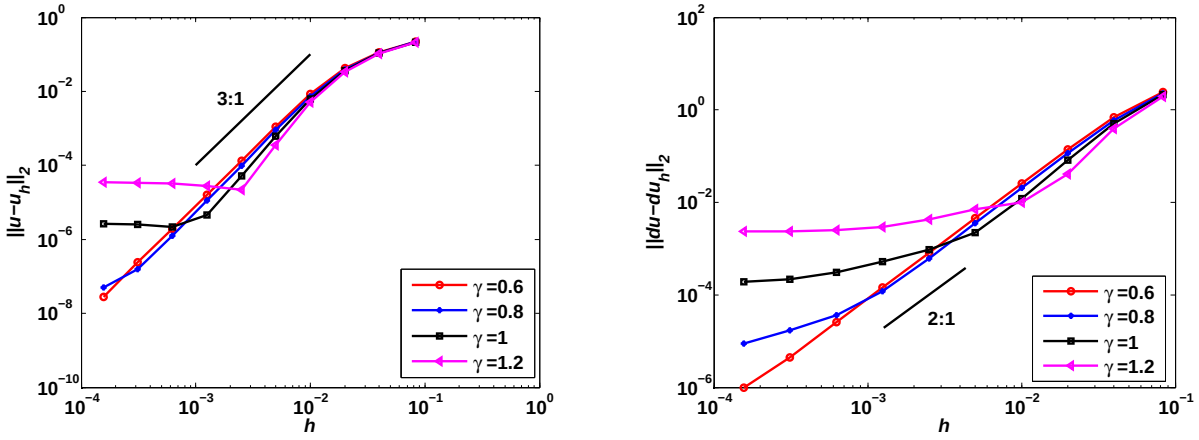

(a) (b)

Figure 3: L^2 norm and Semi-norm H^1 errors of the solution of the fourth order ODE as a function of nodal spacing, with $l_0 = 0.025$ and different values of γ.

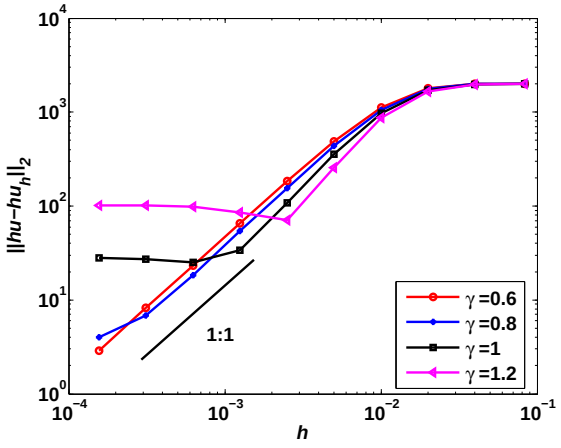

Figure 4: Semi-norm H^2 error of the solution of the fourth order ODE as a function of nodal spacing, with $l_0 = 0.025$ and different values of γ.

4.1.2 Two dimensional domain

Subsequently, we will study the accuracy of the second and fourth order phase-field model to approximate the crack length according to Fig. 5. The Dirichlet condition $v = 0$, for the phase-field on the crack surface Γ is set. There are two sources of errors in the phase-field calculations:

1. The numerical error in approximating the PDE for a fixed l_0, which depends on the nodal spacing h.

2. The modeling error associated with replacing the length of a sharp crack by a regularized functional, which depends on l_0.

We first focus on the first error. The length scale parameter l_0 is considered as a positive parameter to control the size of the fracture zone. When l_0 goes to zero, Γ_{l_0} converges to the discrete fracture surface. A certain minimum mesh size is needed to find the "appropriate" length scale. Here we consider a two dimensional domain Ω with a sharp crack surface $\Gamma = 0.5$ as is shown in the Fig. 5.

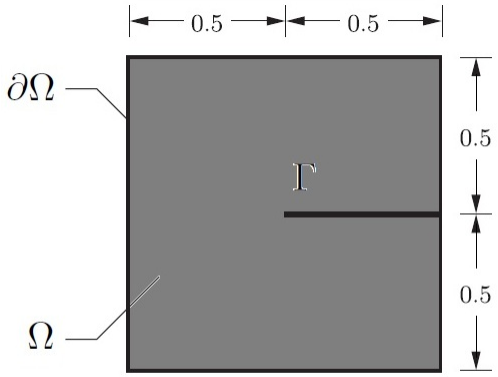

Figure 5: Two dimensional 1×1 square, with a sharp crack surface $\Gamma = 0.5$.

To examine criteria to select l_0 relative to h, we perform calculations with the second and fourth order model for a fixed grid spacing $h = 0.0013$, and vary l_0. We also consider several values of γ. If l_0 is very small relative to the fixed h, then the numerical calculations will not properly resolve the length scale in the model, and the numerical error will be large. If l_0 is too large, the the modeling error may grow. Thus, we expect a tradeoff which selects an optimal l_0 for a given h and γ. As it is obvious from Fig. 6, more accurate results are obtained with smaller length scale parameter for the fourth order approximation. For the second order phase-field model, higher values of γ give better results. For instance, $\gamma = 4.8$ and $2h \leq l_0$ resolves the regularized crack surface such that $\Gamma_{l_0} \approx \Gamma$, while for $\gamma = 1.8$, $4h \leq l_0$ is needed. Hence, in the second order model, as γ increases the results get better and a finer length scale parameter is needed. In the fourth order phase-field approximation model, as γ decreases the results get better. In this case, for all values of γ, choosing $h \leq l_0$ gives reasonable results.

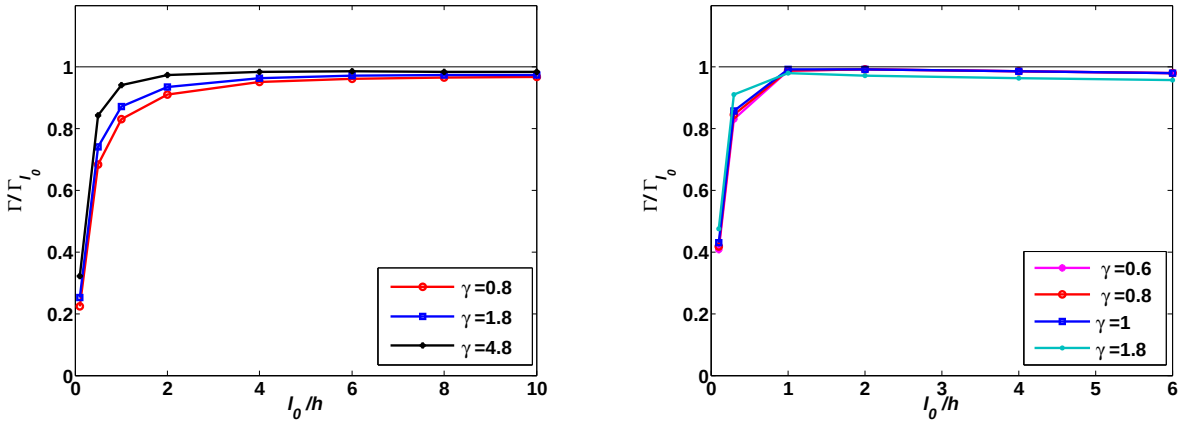

(a) (b)

Figure 6: Exact crack length over approximated crack length versus length scale parameter over nodal spacing, by (a) the second order phase-field model with $\gamma = 0.8, 1.8, 4.8$, (b) the fourth order phase-field model with $\gamma = 0.6, 0.8, 1.0, 1.8$, for $h = 0.0013$.

Next, we examine the convergence in terms of both the modeling and the discretization error. For this, we refine in a concerted way h and l_0 keeping the ratio fixed. Fig. 7 shows the rate of convergence of these two models with $l_0 = 2h$. The second order model with $\gamma = 0.8$ converges much slower than the fourth order model. This is due to the large radius of influence and smoothness of the LME basis functions. Fig. 7 also shows the rate of convergence for the second order model with $\gamma = 4.8$ and $l_0 = 2h$. In this case, the rate of convergence of the second order model is still much lower than the fourth order model with $\gamma = 0.8$ and $l_0 = 2h$.

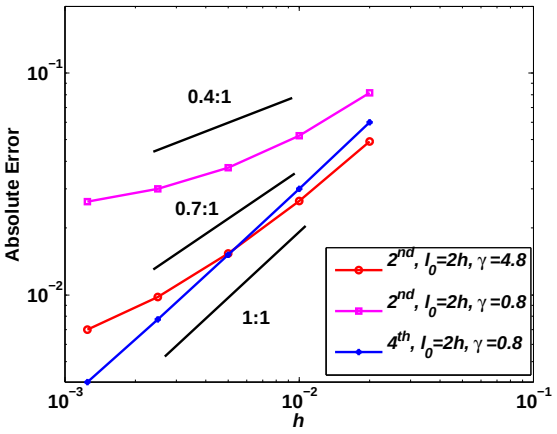

Figure 7: Absolute error of the crack length for the second and fourth order models.

4.2 Mechanical Problems

4.2.1 Infinite plate with a stationary horizontal crack

In order to study the accuracy of the phase-field model, we discuss a benchmark problem that has an exact solution. Consider an infinite plate with a horizontal crack of length 2a = 20mm under a remote uniform stress field σ as shown in Fig. 8. The analytical solution near the crack tip for the stress fields and displacement in terms of local polar coordinates from the crack tip are [44].

$$u_x(r,\theta) = \frac{2(1+\upsilon)}{\sqrt{2\pi}} \frac{K_I}{E} \sqrt{r} \cos(\frac{\theta}{2}) \left(2 - 2\upsilon - \cos^2(\frac{\theta}{2})\right), \tag{38}$$

$$u_y(r,\theta) = \frac{2(1+\upsilon)}{\sqrt{2\pi}} \frac{K_I}{E} \sqrt{r} \sin(\frac{\theta}{2}) \left(2 - 2\upsilon - \cos^2(\frac{\theta}{2})\right), \tag{39}$$

Where $K_I = \sigma\sqrt{\pi a}$ is the stress intensity factor, υ is Poisson's ratio and E is Young's modulus.

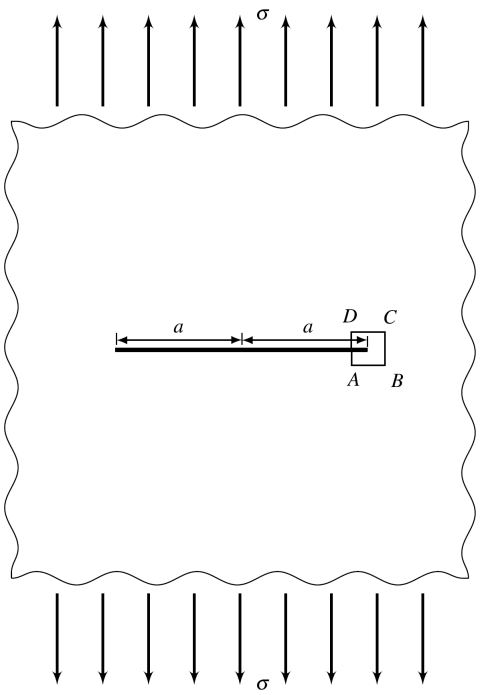

Figure 8: Infinite plate with a center crack under uniform tension and modeled geometry ABCD.

The analytical solution is valid for a region close enough to the crack tip. So, we consider a square ABCD of length 1mm × 1mm, $E = 10^7 \text{N/mm}^2$, $\upsilon = 0.3$, $\sigma = 10^4 \text{N/mm}^2$ and the modeled crack length is 0.5mm. Plane strain state is assumed. Dirichlet boundary conditions are imposed on the edges and the crack does not propagate. As we mentioned, LME basis functions satisfy a weak Kronecker delta property. This property allows us to impose Dirichlet boundary conditions by computing a node-based interpolant or an L^2 projection of the boundary data. In order to introduce the pre-crack, on the crack surface, we impose the Dirichlet condition $v = 0$ for the crack phase-field. We first solve a linear system for the v-field, subsequently we solve the elastic linear system for $\boldsymbol{u}$. For stationary cracks, the phase-field value is not updated. Fig. 9a indicates the error in the $L2$ displacement norm for different length scale parameter for the finite element method, the second and fourth order methods with $\gamma = 4.8$ and $\gamma = 1.0$, respectively. Choosing $2h \leq l_0 < 4h$ and $l_0 \geq 8h$ for the fourth and second order model, respectively, gives the best approximation of the solution (for $h = 0.005$). As mentioned before, this figure also illustrates almost the same results for FEM and the second order method with $\gamma = 4.8$. In this case, the value of the length scale parameter, for the second order model and FEM, is large. In other words, a fine discretization is needed to resolve the crack, if small length scale parameter is required. Fig. 9b shows the $L2$ norm error versus h for different discretization. The best rate of convergence is obtained for the fourth order phase-field model with $\gamma = 1.0$ and $l_0 \geq 2h$. The convergence rate of 0.63 is poor. However, the phase-field model cannot capture the jump in the displacement field and the analytic crack opening as discrete crack approaches such as XFEM. In this view, the convergence rate of the fourth order model is surprisingly good.

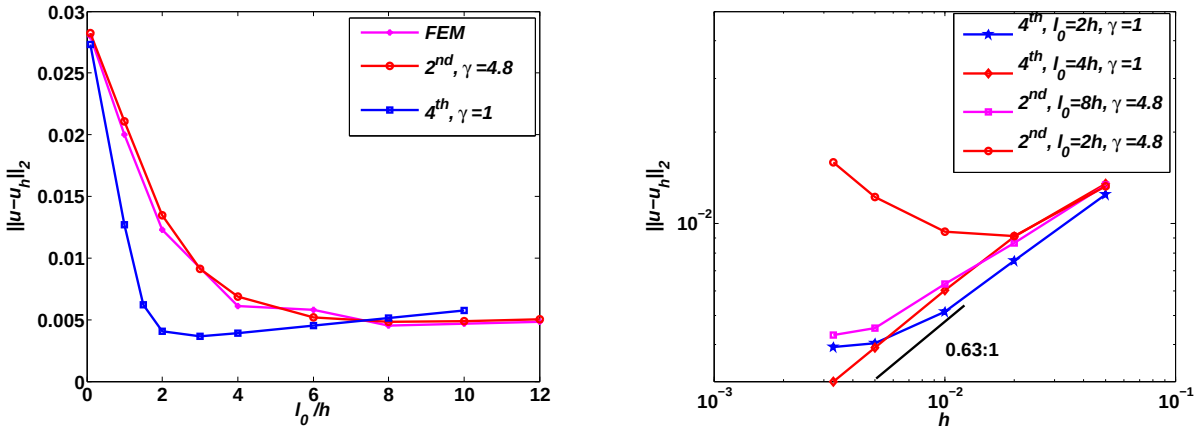

(a) (b)

Figure 9: (a) L^2 norm Error for $h = 0.005$, and different values of l_0, (b) L^2 norm Error versus different discretization.

4.2.2 Crack propagation in a cantilever beam

Consider the two-dimensional cantilever beam problem under plane strain condition [18, 39]. The geometric setup is indicated in Fig. 11. In order to avoid rigid body motion, we fix the point $x = 1, y = 0.5$ and the left ends are displaced as shown in Fig. 11. The material properties used for the analysis are $E = 10^9$ N/mm^2, Poisson's ratio $\nu = 0.3$, critical energy release rate $G_c = 1000$ N/mm and $k = 10^{-6}$. Constant displacement increments $\Delta u = 0.6 \times 10^{-6}$ mm, are used for each step of computation. For computational efficiency, the discretization is refined only in the area where the crack is expected to propagate. We also study the effects of the length scale parameter. Fig. 12 shows that mesh-independent results are achieved when refining the discretization. For $h = 0.0015$, the influence of the length scale parameter on the global response of these two models, is analyzed in Fig. 13. For the fourth order model, $l_0 \geq 4h$, is needed in order to obtain a nearly identical peak load and post-peak curve. While for the second order model $l_0 \geq 12h$ is needed. In other words, the second order model is more sensitive with respect to the length scale. The crack path at different stages is illustrated in Fig. 14. As it was expected , the crack propagates straight [39].

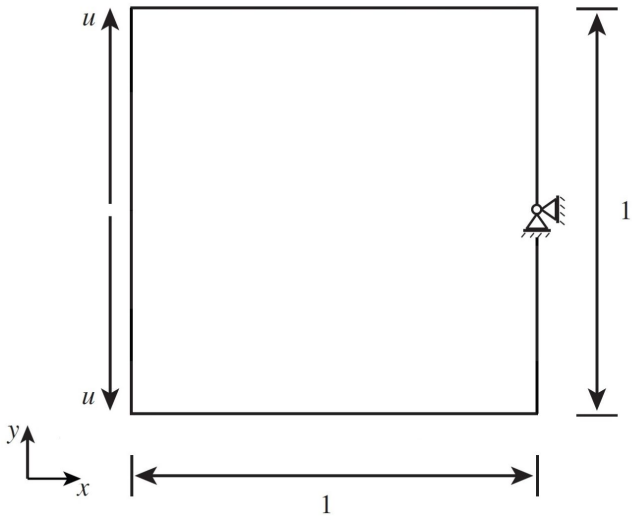

Figure 10: The geometry and boundary conditions of a square beam of side length $L = 1$ mm.

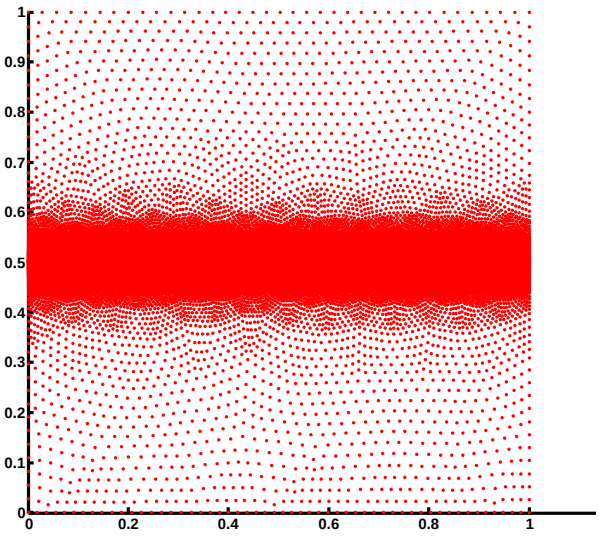

Figure 11: The nodal discretization of 60931 number of nodes.

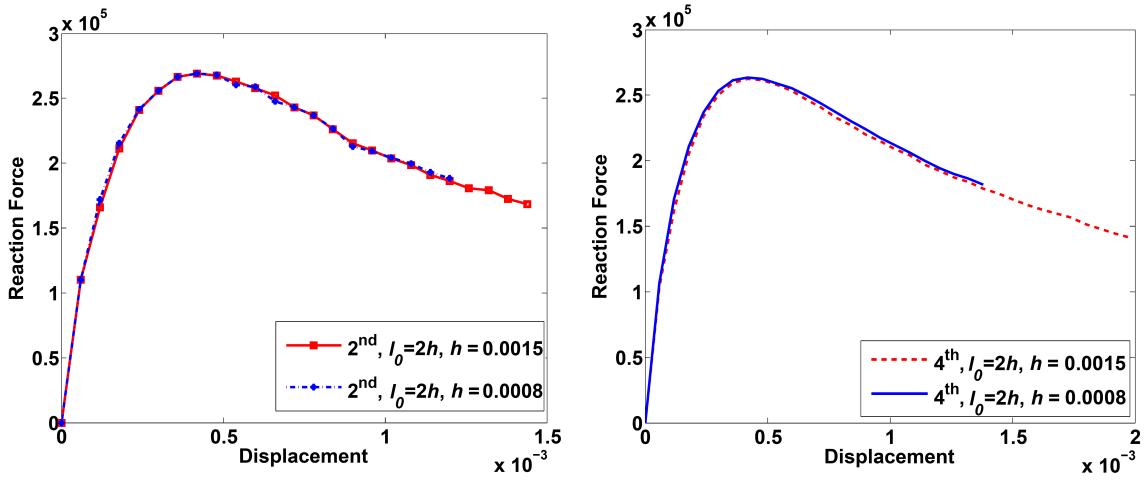

(a) (b)

Figure 12: Load-deflection curves of (a) the second order model with $\gamma = 4.8$, (b) the fourth order model with $\gamma = 1.0$, $l_0 = 2h$, $h = 0.0015, 0.0008$ and 15274, 60931 nodes respectively.

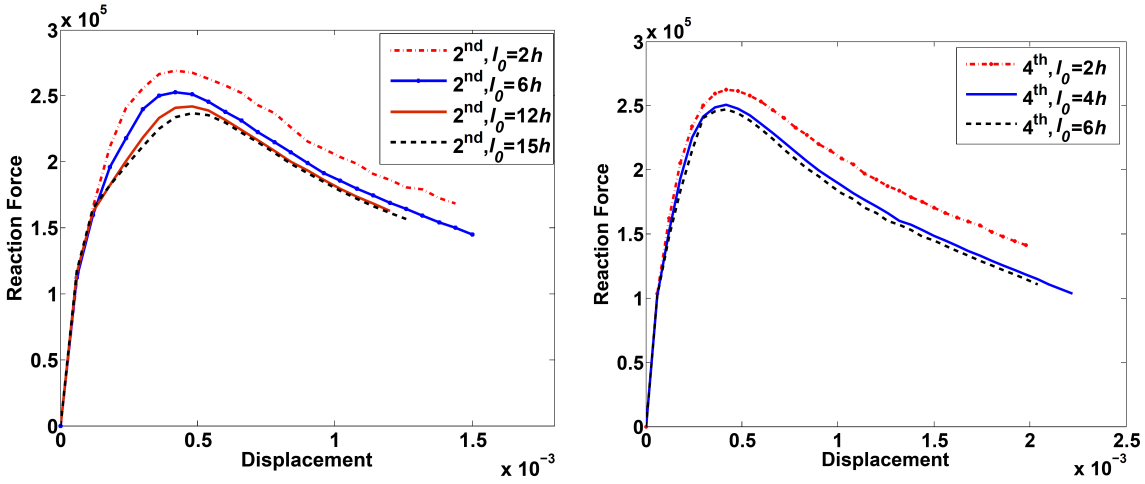

(a) (b)

Figure 13: (a) Load-deflection curves of the second order method for different values of l_0, fixed value $h = 0.0015$ and $\gamma = 4.8$. (b) Load-deflection curves of the fourth order model for different values of l_0, fixed value $h = 0.0015$ and $\gamma = 1.0$.

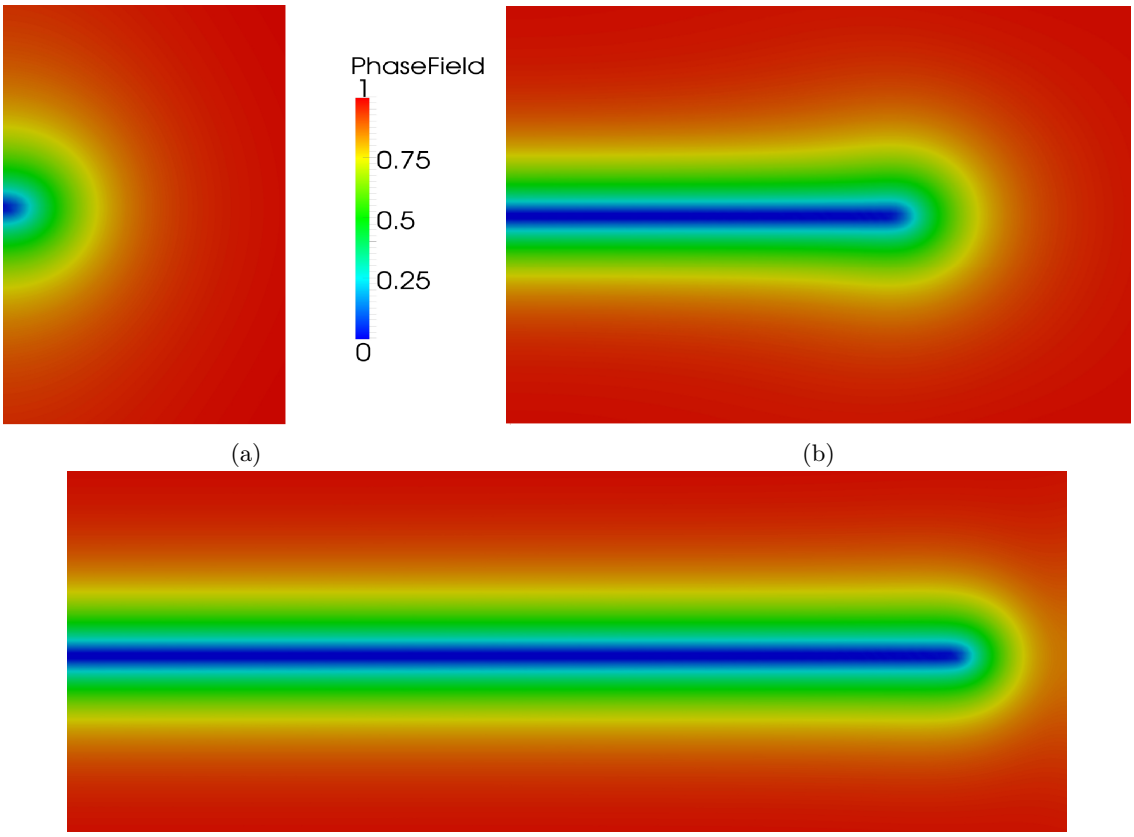

Figure 14: Close up around the crack path at the three stages of evolution.

4.2.3 Three-dimensional tension test

A similar problem is now solved in three dimensions as is illustrated in Fig. 15. The geometry and the boundary conditions are given in Fig. 15 as well. In order to avoid rigid body motion, the line $x = 0, y = 2.5$ and the point $x = 0, y = 2.5, z = 0.5$ are fixed. The material parameters are: Young's modulus $E = 10^9$ N/mm^2, Poisson's ratio $\nu = 0.3$ and fracture energy $G_c = 100$ N/mm. Constant displacement increments $\Delta u = 1.5 \times 10^{-5}$mm are applied at each load step. Numerical integration is performed over an unstructured background mesh of linear tetrahedral elements. The discretization is refined in an area where the crack is expected to propagate, see Fig. 16. The crack propagation path is illustrated in Figs. 17 and 18 for an effective nodal spacing of $h = 0.06$. As it was expected, the crack propagates in the symmetry path [39]. Figs. 19 and 20 show the load-deflection curves for different discretization. Fig. 21 illustrate the load-deflection curves for different values of G_c.

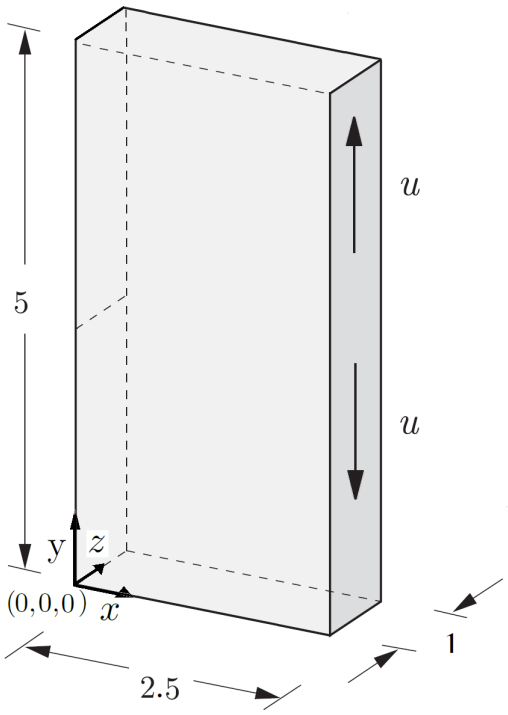

Figure 15: Geometry, loading and boundary condition for the three-dimensional mode-I tension test.

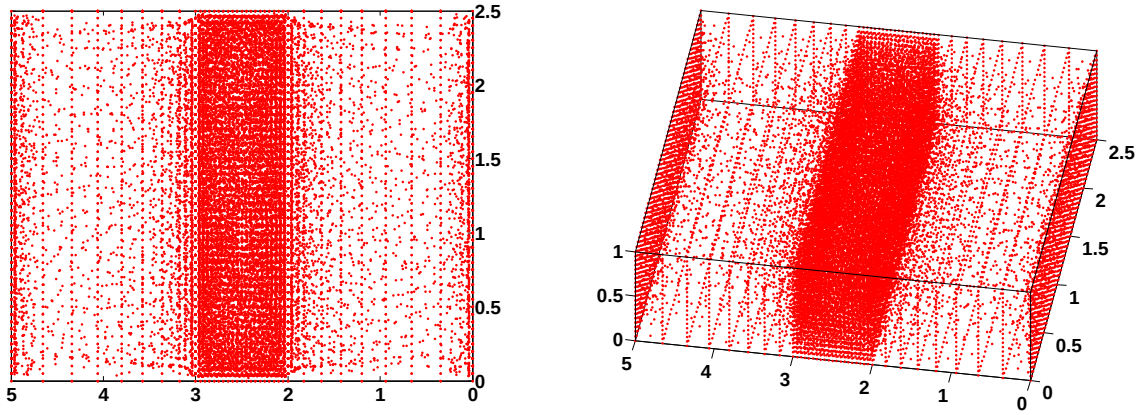

(a) (b)

Figure 16: The nodal discretization is much finer around the expected crack path.

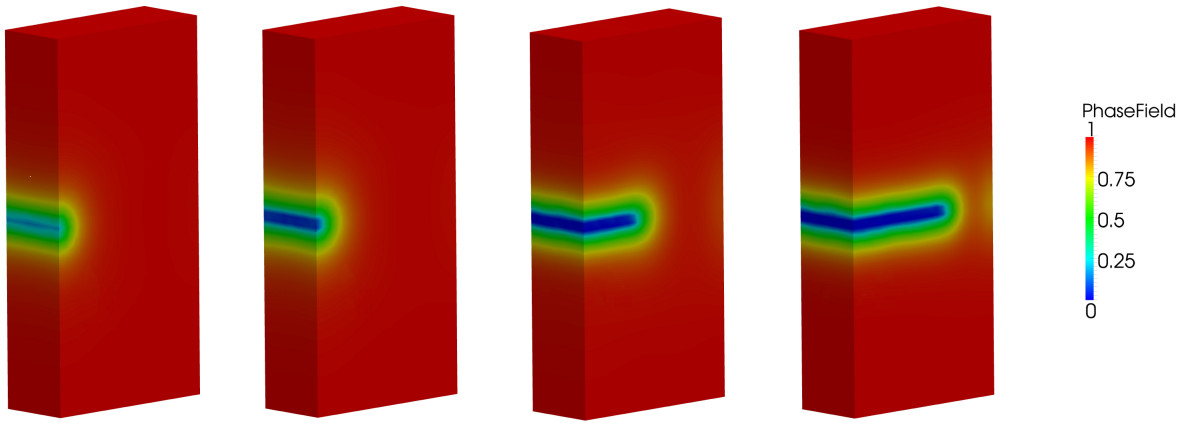

Figure 17: The crack path at the four stages of evolution.

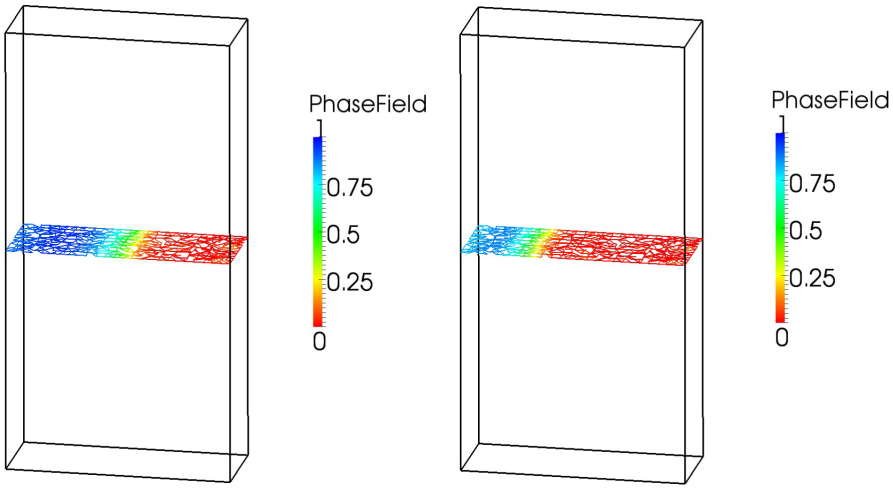

Figure 18: Phase filed results on the cross section plane $y = 2.5$ to indicate crack path inside the body.

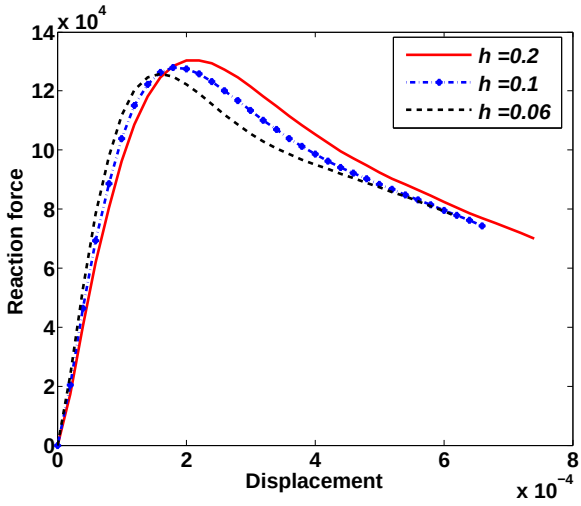

Figure 19: Load-deflection curves of the second order method with $\gamma = 4.8$, $l_0 = 0.414$ and different refinement with $1661, 14453, 28177$ number of nodes respectively.

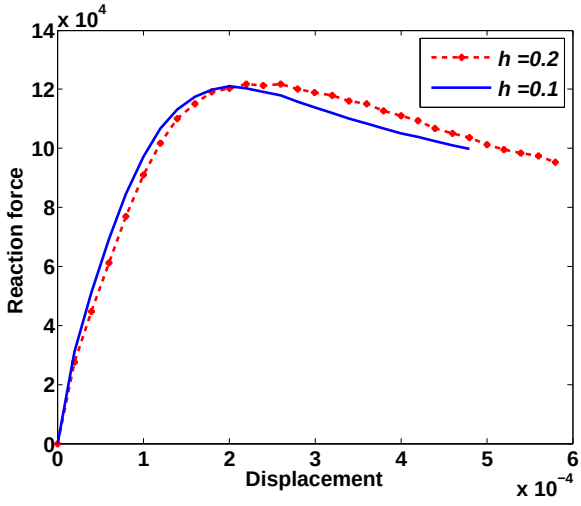

Figure 20: Load-deflection curves of the fourth order method with $\gamma = 1.0$, $l_0 = 0.414$ and different refinement.

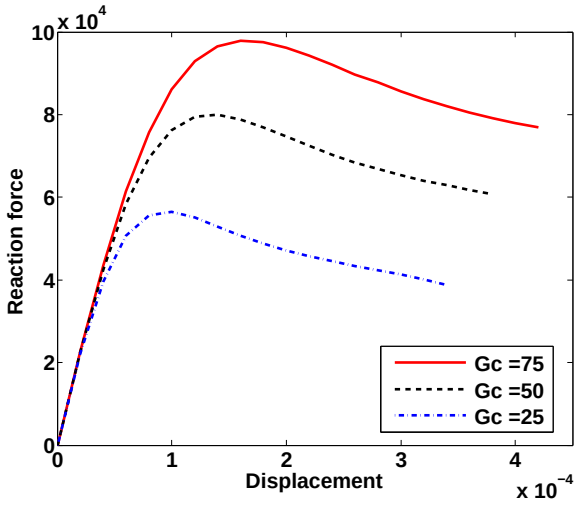

Figure 21: Reaction force-displacement curves for the fourth order model with $h = 0.1$, $l_0 = 0.414$, $\gamma = 1.8$ and different values of G_c.

4.2.4 Single edge notched beam with initial crack

In this example we study a slanted crack propagation problem. The initial crack, all relevant mechanical properties, boundary conditions and the dimensions are shown in Fig. 22. In this figure, the coordinates or location of point A $= (37.5, 150, 0)$. A candidate v-field is postulated with initial crack width of $2h$. We also consider the regularization parameter, approximatively two times the effective nodal spacing. The results are shown in Figs. 24, 25 and 26, for an effective nodal spacing $h = 2.6$mm. The discretization is refined around the expected crack path, see Fig. 23. The constant displacement increments $\Delta u = 10^{-3}$mm, are applied for each step of computation. The crack propagation path is illustrated in Figs. 24, 25. In Fig. 25, the crack path for the second and fourth order model is compared with the experimental result in [29]. The load displacement curves are shown in Fig. 26 for both phase-field models, XFEM [7] containing 46380 elements and experimental results in [29].

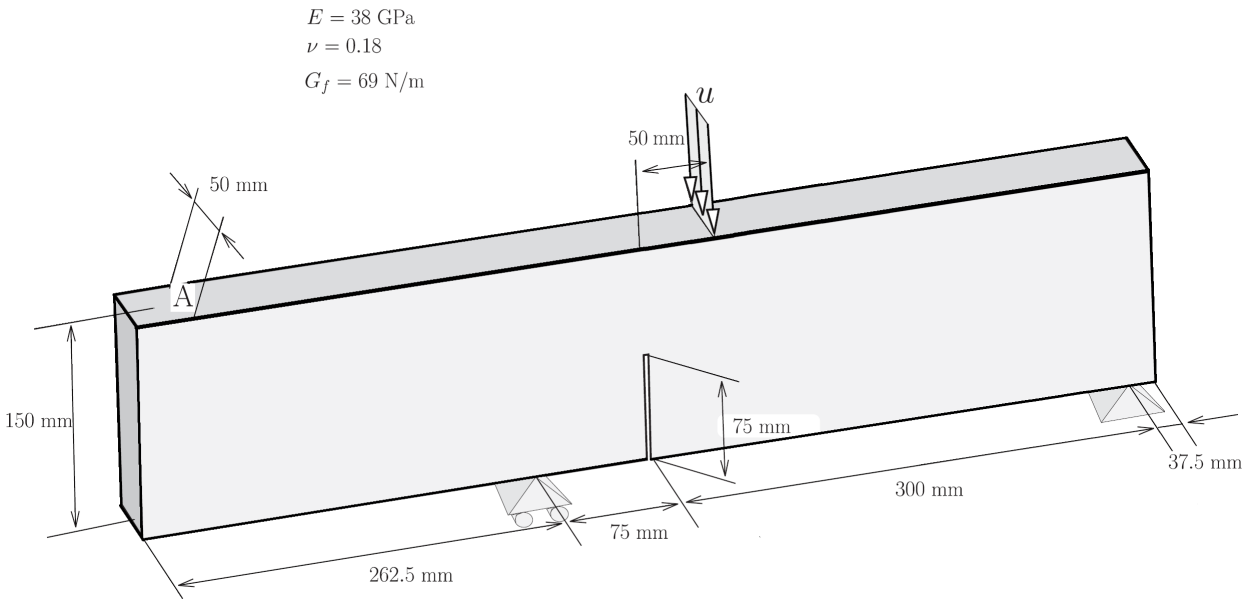

Figure 22: Geometry, loading and boundary condition for the three-dimensional single edge notched beam.

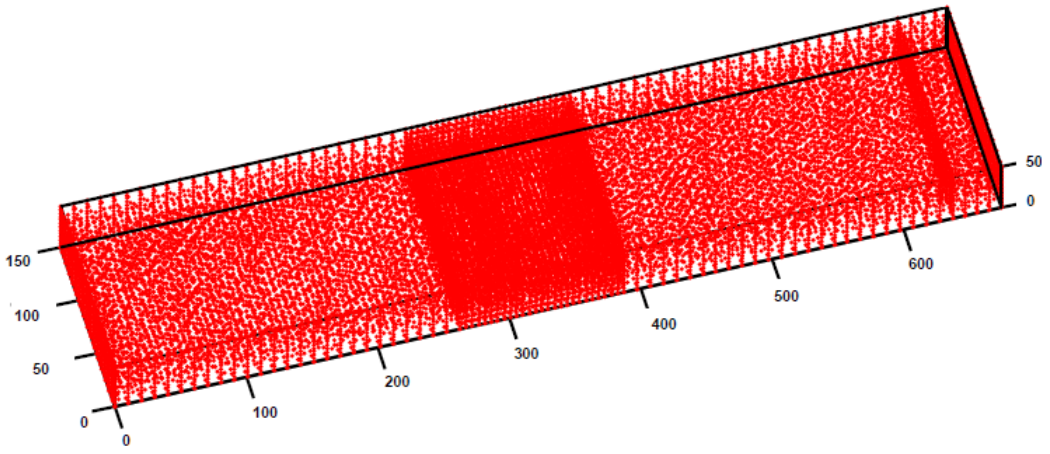

Figure 23: The nodal discretization is used to compute the results for the three-dimensional single edge notched beam.

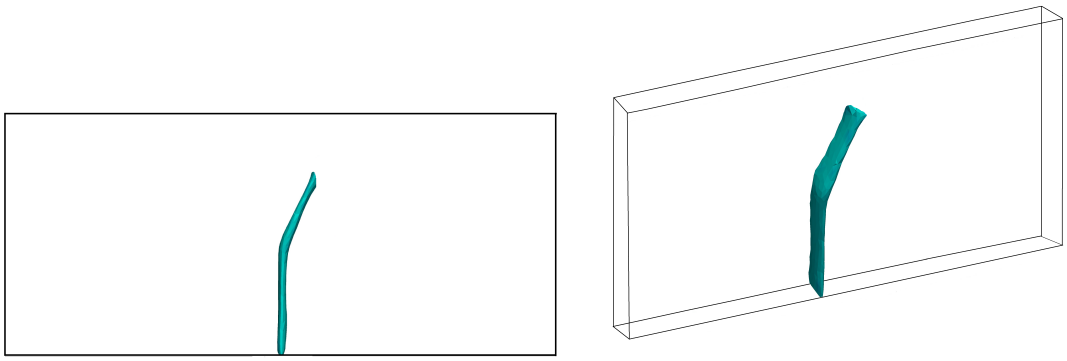

(a) (b)

Figure 24: The crack path at two different views.

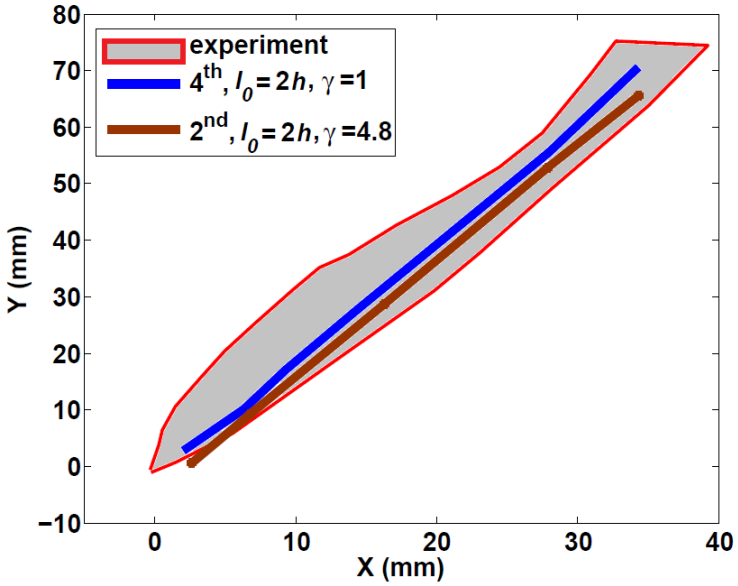

Figure 25: Crack path for the fourth and the second order phase-field methods with $\gamma = 1.0$ and $\gamma = 4.8$ respectively, compared with the experiments in [29].

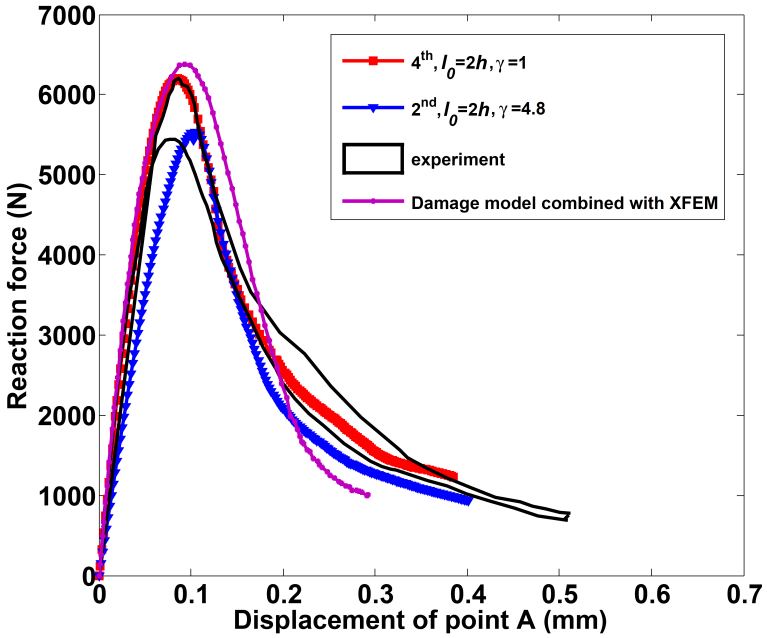

Figure 26: Reaction force displacement curve for point A, compared with [7, 29].

4.2.5 Non-planar crack growth

In this example, we consider a beam under bending which involves non-planar crack growth. The beam dimensions and the boundary condition are shown in Fig. 27. The beam is notched at an angle $\alpha = 45°$ versus the x-axis, see Fig. 27. This example was also studied with the extended finite element method in [27] and meshfree method in [57]. They show that the crack surface, while propagating downwards, becomes finally orthogonal to the xz-plane.

We study the phase-field method with numerical integration of an unstructured background mesh of 65456 tetrahedrons with the effective nodal spacing $h = 0.0018$ and $l_0 = 4h$. Here also discretization is refined in an area where the crack is expected to propagate, see Fig. 28. Fig. 29 illustrates the evolution of the crack front from a top view for the fourth order phase-field method with $\gamma = 1.8$. The crack grows downwards and becomes orthogonal to the xz-plane. Fig. 30 shows the evolution of the crack front from a side view. The results are in good agreement with the results obtained in [27, 57]. Similar results are obtained for the second order phase-field model with $\gamma = 4.8$. The acceptable results have been obtained in [57], for 570000 and 4400000 particles (540000 and 4300000 stress points, respectively) and 65000 and 210000 particles for adaptive scheme.

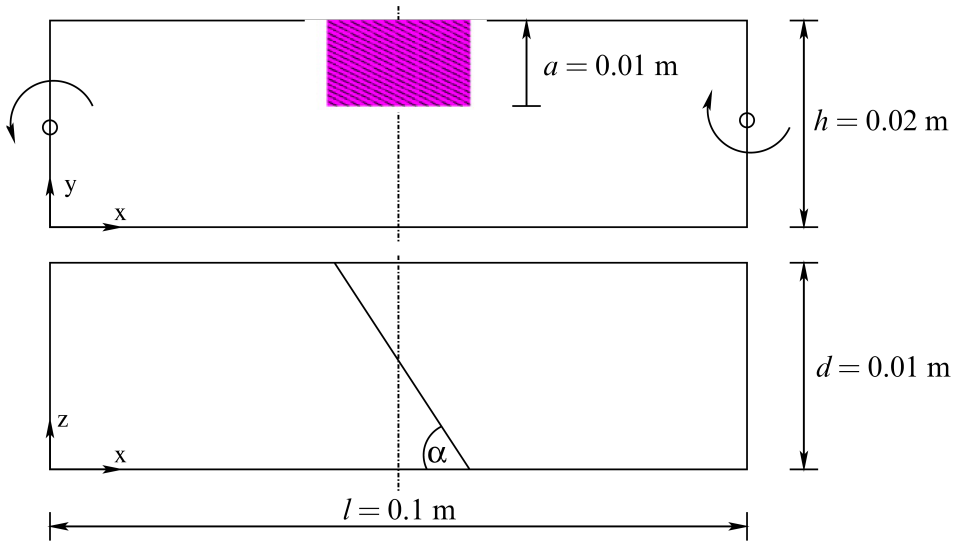

Figure 27: Side and top views of the beam with an initial crack for the non-planar crack growth.

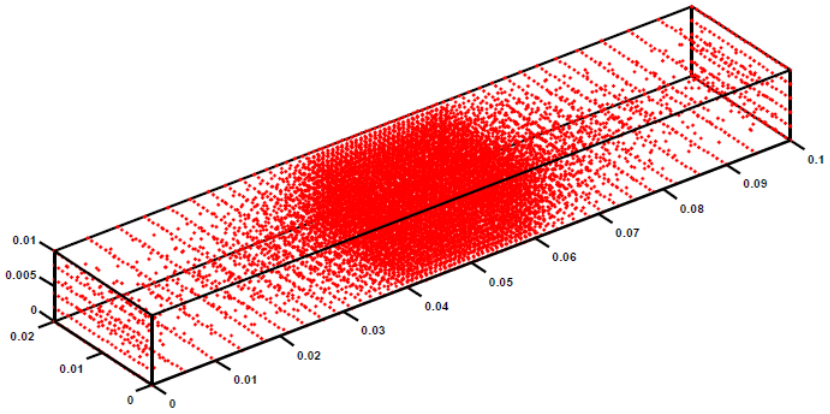

Figure 28: The nodal discretization is used to compute the results for the non-planar crack growth.

Figure 29: Evolution of the crack front in the beam seen from the top, the maximum and the minimum of phase-field, i.e. $v = 1$ and $v = 0$ are shown.

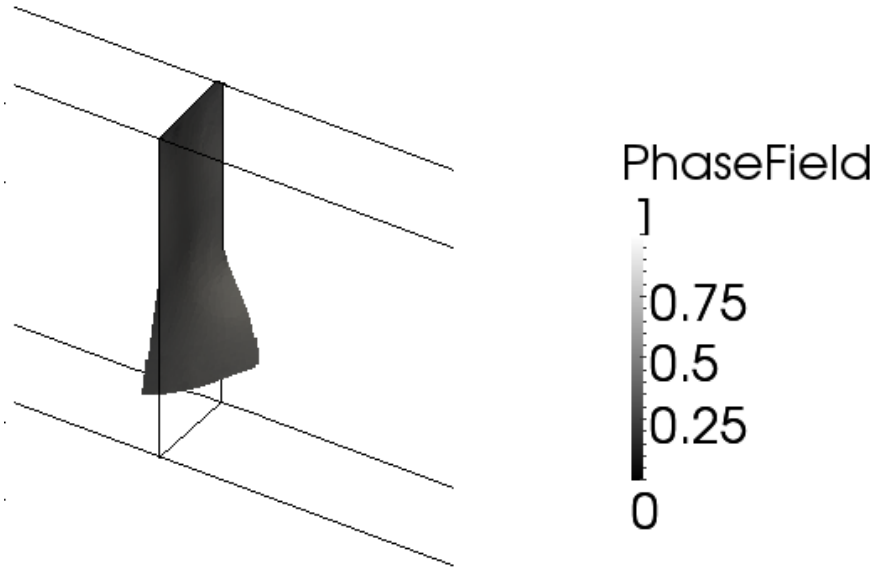

(a)

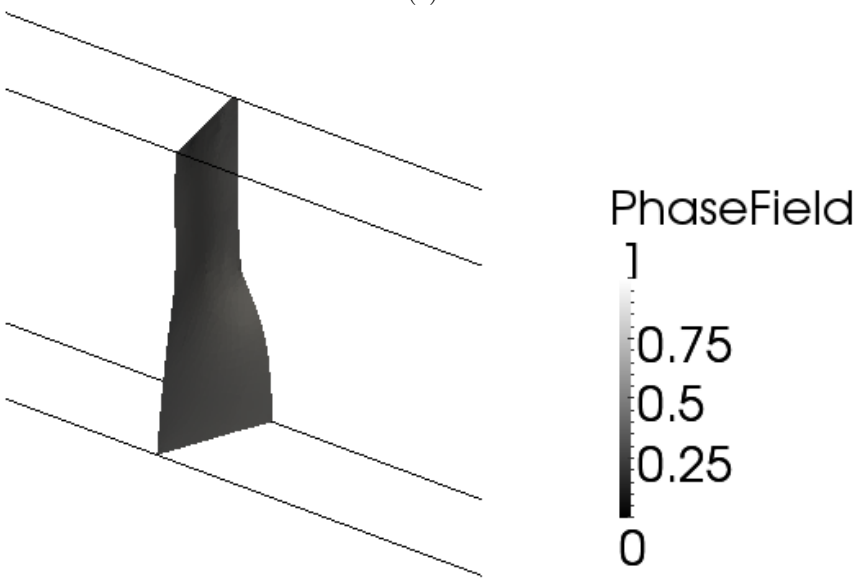

(b)

Figure 30: The crack path at the different stages of evolution from a side view, the maximum and the minimum of phase-field, i.e. $v = 1$ and $v = 0$ are shown.

5 Conclusions

We have applied a fourth order phase-field model in combination with smooth LME approximants. The smoothness and higher order continuity of the LME approximants i.e. C^∞, allows to directly solve the fourth order phase-field equation without splitting it into two second order differential equations. The LME approximants able us to use highly non uniform meshes and local refinement, and that by using this numerical treatment the expressions appearing during the Ritz-Galerkin variational formulation are easy to obtain and not require a cumbersome treatment unlike discontinous Galerking based methods. We compared the second and the fourth order phase-field model. The fourth order phase-field model gives more accurate and efficient results with lower γ. We conclude that there is an optimal value of $\gamma \leq 1.8$ for the fourth order phase-field model and $\gamma \geq 4.8$ for the second order phase-field model that maximizes the accuracy. We have also shown that both the second and fourth order phase-field models are capable of capturing complex crack behavior in three dimensions. The proposed approximation also shows potential for other problems which will be examined in the future, such as cracks in thin shell bodies with complex geometry and topology.

Acknowledgements

Fatemeh Amiri and Timon Rabczuk would like to thank the DAAD Programme des Projektbezogenen Personenaustauschs, for financial support to trip to Spain, and the Free State of Thuringia and Bauhaus Research School for financial support during the duration of this project.

References

[1] Numerical simulations of 3-d cracks using coupled efgm and fem. *International Journal for Computational Methods in Engineering Science and Mechanics*, 15:227 – 231, 2014.

[2] L. Ambrosio. Variational problems in sbv and image segmentation. *Acta Applicandae Mathematica*, 17(1):1–40, 1989.

[3] L. Ambrosio and V. M. Tortorelli. Approximation of functionals depending on jumps by elliptic functionals via -convergence. *Communications on Pure and Applied Mathematics*, 43(8):999–1036, 1990.

[4] F. Amiri, C. Anitescu, M. Arroyo, S.P.A. Bordas, and T. Rabczuk. Xlme interpolants, a seamless bridge between xfem and enriched meshless methods. *Computational Mechanics*, 53(1):45–57, 2014.

[5] F. Amiri, D. Millán, Y. Shen, T. Rabczuk, and M. Arroyo. Phase-field modeling of fracture in linear thin shells. *Theoretical and Applied Fracture Mechanics*, 69(0):102 – 109, 2014.

[6] A. Apostolatos, R. Schmidt, R. Wüchner, and K-U. Bletzinger. A nitsche-type formulation and comparison of the most common domain decomposition methods in isogeometric analysis. *International Journal for Numerical Methods in Engineering*, 97(7):473–504, 2014.

[7] P. Areias and T. Belytschko. Analysis of three-dimensional crack initiation and propagation using the extended finite element method. *International Journal for Numerical Methods in Engineering*, 63(5):760–788, 2005.

[8] P. Areias and T. Rabczuk. Finite strain fracture of plates and shells with configurational forces and edge rotations. *International Journal for Numerical Methods in Engineering*, 94(12):1099–1122, 2013.

[9] P. Areias, T. Rabczuk, and P.P. Camanho. Finite strain fracture of 2d problems with injected anisotropic softening elements. *Theoretical and Applied Fracture Mechanics*, 72:50 – 63, 2014. Multiscale Modeling of Material Failure.

[10] P. Areias, T. Rabczuk, and D. Dias da Costa. Element-wise fracture algorithm based on rotation of edges. *Engineering Fracture Mechanics*, 110:113 – 137, 2013.

[11] M. Arroyo and M. Ortiz. Local maximum-entropy approximation schemes: a seamless bridge between finite elements and meshfree methods. *International Journal for Numerical Methods in Engineering*, 65(13):2167–2202, 2006.

[12] Z. Bazant. Imbricate continuum and its variational derivation. *Journal of Engineering Mechanics*, 110(12):1693–1712, 1984.

[13] Z. Bazant and T.P Chang. Instability of nonlocal continuum and strain averaging. *Journal of Engineering Mechanics*, 110(10):1441–1450, 1984.

[14] Z. Bazant and M. Jirásek. Nonlocal integral formulations of plasticity and damage: Survey of progress. *Journal of Engineering Mechanics*, 128(11):1119–1149, 2002.

[15] Z. Bazant and F.B. Lin. Nonlocal smeared cracking model for concrete fracture. *Journal of Structural Engineering*, 114(11):2493–2510, 1988.

[16] T. Belytschko and T. Black. Elastic crack growth in finite elements with minimal remeshing. *International Journal for Numerical Methods in Engineering*, 45(5):601–620, 1999.

[17] G. Bhardwaj, I.V. Singh, B.K. Mishra, and T.Q. Bui. Numerical simulation of functionally graded cracked plates using {NURBS} based {XIGA} under different loads and boundary conditions. *Composite Structures*, 126:347 – 359, 2015.

[18] M. J. Borden, T. J. R. Hughes, C. M. Landis, and C. V. Verhoosel. A higher-order phase-field model for brittle fracture: Formulation and analysis within the isogeometric analysis framework. *Computer Methods in Applied Mechanics and Engineering*, 273(0):100 – 118, 2014.

[19] M. J. Borden, C. V. Verhoosel, M. A. Scott, T. J. R. Hughes, and C. M. Landis. A phase-field description of dynamic brittle fracture. *Computer Methods in Applied Mechanics and Engineering*, 217-220:77–95, 2012.

[20] B. Bourdin. Numerical implementation of the variational formulation for quasi-static brittle fracture. *Interfaces and Free Boundaries*, 9(3):411–430, 2007.

[21] B. Bourdin, G.A. Francfort, and J.-J. Marigo. The Variational Approach to Fracture. *Journal of Elasticity*, 91(1-3):5–148, 2008.

[22] K. Chaoui, R. Khelif, N. Zeghib, and A. Chateauneuf. Failure analysis of polyethylene gas pipes. In Guy Pluvinage and MohamedHamdy Elwany, editors, *Safety, Reliability and Risks Associated with Water, Oil and Gas Pipelines*, NATO Science for Peace and Security Series, pages 131–163. Springer Netherlands, 2008.

[23] R. de Borst. *Damage, Material Instabilities, and Failure*, pages 22–234. John Wiley and Sons, Ltd, 2004.

[24] de Borst, R. , Benallal, A., and Heeres, O. M. . A gradient-enhanced damage approach to fracture. *Journal de Physique Archives IV France*, 06:C6–491–C6–502, 1996.

[25] G.A. Francfort and J.-J. Marigo. Revisiting brittle fracture as an energy minimization problem. *Journal of the Mechanics and Physics of Solids*, 46:1319–1342, 1998.

[26] S.Sh. Ghorashi, N. Valizadeh, S. Mohammadi, and T. Rabczuk. T-spline based {XIGA} for fracture analysis of orthotropic media. *Computers and Structures*, 147:138 – 146, 2015.

[27] A. Gravouil, N. Moës, and T. Belytschko. Non-planar 3d crack growth by the extended finite element and level setspart ii: Level set update. *International Journal for Numerical Methods in Engineering*, 53(11):2569–2586, 2002.

[28] A. A. Griffith. The phenomena of rupture and flow in solids. *Philosophical Transactions of the Royal Society of London. Series A, Containing Papers of a Mathematical or Physical Character*, 221(582-593):163–198, 1921.

[29] J.C. Glvez, M. Elices, G.V. Guinea, and J. Planas. Mixed mode fracture of concrete under proportional and nonproportional loading. *International Journal of Fracture*, 94(3):267–284, 1998.

[30] F. E. Hildebrand and C. Miehe. A phase field model for the formation and evolution of martensitic laminate microstructure at finite strains. *Philosophical Magazine*, 92(34):4250–4290, 2012.

[31] M. Hofacker and C. Miehe. Continuum phase field modeling of dynamic fracture: variational principles and staggered fe implementation. *International Journal of Fracture*, 178(1-2):113–129, 2012.

[32] M. Hofacker and C. Miehe. A phase field model of dynamic fracture: Robust field updates for the analysis of complex crack patterns. *International Journal for Numerical Methods in Engineering*, 93(3):276–301, 2013.

[33] T.J.R. Hughes. *The Finite Element Method: Linear Static and Dynamic Finite Element Analysis*. Dover Civil and Mechanical Engineering. Dover Publications, 2012.

[34] GR. Irwin. Elasticity and plasticity: fracture. *In Encyclopedia of Physics, Fl gge S (ed.), Springer: Berlin*, 6:551–590, 1958.

[35] S. Li and W.K. Liu. Meshfree and particle methods and their applications. *Applied Mechanics Reviews*, 55(1):1–34, 2002.

[36] J. Liang, Z. Zhang, J.H. Prévost, and Z. Suo. Time-dependent crack behavior in an integrated structure. *International Journal of Fracture*, 125(3-4):335–348, 2004.

[37] C. Miehe, M. Hofacker, and F. Welschinger. A phase field model for rate-independent crack propagation: Robust algorithmic implementation based on operator splits. *Computer Methods in Applied Mechanics and Engineering*, 199(4548):2765 – 2778, 2010.

[38] C. Miehe and L. M. Schänzel. Phase field modeling of fracture in rubbery polymers. part i: Finite elasticity coupled with brittle failure. *Journal of the Mechanics and Physics of Solids*, 65:93 – 113, 2014.

[39] C. Miehe, F. Welschinger, and M. Hofacker. Thermodynamically consistent phase-field models of fracture: Variational principles and multi-field fe implementations. *International Journal for Numerical Methods in Engineering*, 83:1273–1311, 2010.

[40] D. Millán, A. Rosolen, and M. Arroyo. Thin shell analysis from scattered points with maximum-entropy approximants. *International Journal for Numerical Methods in Engineering*, 85(6):723–751, 2011.

[41] D. Millán, A. Rosolen, and M. Arroyo. Nonlinear manifold learning for meshfree finite deformations thin shell analysis. *International Journal for Numerical Methods in Engineering*, 93(7):685–713, 2013.

[42] N. Moës, J. Dolbow, and T. Belytschko. A finite element method for crack growth without remeshing. *International Journal for Numerical Methods in Engineering*, 46(1):131–150, 1999.

[43] D. Mumford and J. Shah. Optimal approximations by piecewise smooth functions and associated variational problems communications on pure and applied mathematics. *Communications on Pure and Applied Mathematics*, 42(5):577–685, 1989.

[44] V. P. Nguyen, T. Rabczuk, S. Bordas, and M. Duflot. Meshless methods: A review and computer implementation aspects. *Mathematics and Computers in Simulation*, 79(3):763 – 813, 2008.

[45] N. Nguyen-Thanh, N. Valizadeh, M.N. Nguyen, H. Nguyen-Xuan, X. Zhuang, P. Areias, G. Zi, Y. Bazilevs, L. De Lorenzis, and T. Rabczuk. An extended isogeometric thin shell analysis based on kirchhofflove theory. *Computer Methods in Applied Mechanics and Engineering*, 284:265 – 291, 2015. Isogeometric Analysis Special Issue.

[46] H. Nguyen-Xuan, G.R. Liu, S. Bordas, S. Natarajan, and T. Rabczuk. An adaptive singular es-fem for mechanics problems with singular field of arbitrary order. *Computer Methods in Applied Mechanics and Engineering*, 253:252 – 273, 2013.

[47] A. Ortiz, M.A. Puso, and N. Sukumar. Maximum-entropy meshfree method for compressible and near-incompressible elasticity. *Computer Methods in Applied Mechanics and Engineering*, 199(25–28):1859—1871, 2010.

[48] A. Ortiz, M.A. Puso, and N. Sukumar. Maximum-entropy meshfree method for incompressible media problems. *Finite Elements in Analysis and Design*, 47(6):572–585, 2011.

[49] M Pant, I. V. Singh, and B. K. Mishra. A numerical study of crack interactions under thermo-mechanical load using efgm. *Journal of Mechanical Science and Technology*, 25(2):403–413, 2011.

[50] M. Pant, I.V. Singh, and B.K. Mishra. Numerical simulation of thermo-elastic fracture problems using element free galerkin method. *International Journal of Mechanical Sciences*, 52(12):1745 – 1755, 2010.

[51] M. Pant, I.V. Singh, and B.K. Mishra. Evaluation of mixed mode stress intensity factors for interface cracks using {EFGM}. *Applied Mathematical Modelling*, 35(7):3443 – 3459, 2011.

[52] M. Pant, I.V. Singh, and B.K. Mishra. A novel enrichment criterion for modeling kinked cracks using element free galerkin method. *International Journal of Mechanical Sciences*, 68:140 – 149, 2013.

[53] H. Pathak, A. Singh, I.V. Singh, and M. Brahmankar. Three-dimensional stochastic quasi-static fatigue crack growth simulations using coupled fe-efg approach. *Computers and Structures*, 160:1 – 19, 2015.

[54] R. H. J. Peerings, R. de Borst, W. A. M. Brekelmans, and J. H. P. de Vree. Gradient enhanced damage for quasi-brittle materials. *International Journal for Numerical Methods in Engineering*, 39(19):3391–3403, 1996.

[55] R.H.J. Peerlings, R. de Borst, W.A.M. Brekelmans, J.H.P. de Vree, and I. Spee. Some observations on localisation in non-local and gradient damage models. *European Journal of Mechanics A: Solids*, 15(6):937–953, 1996.

[56] T. Rabczuk and T. Belytschko. Cracking particles: a simplified meshfree method for arbitrary evolving cracks. *International Journal for Numerical Methods in Engineering*, 61(13):2316–2343, 2004.

[57] T. Rabczuk and T. Belytschko. A three-dimensional large deformation meshfree method for arbitrary evolving cracks. *Computer Methods in Applied Mechanics and Engineering*, 196(2930):2777 – 2799, 2007.

[58] T. Rabczuk, S. Bordas, and G. Zi. On three-dimensional modelling of crack growth using partition of unity methods. *Computers and Structures*, 88(2324):1391 – 1411, 2010. Special Issue: Association of Computational Mechanics United Kingdom.

[59] R.P. Reed, United States. National Bureau of Standards, and Battelle Memorial Institute. Columbus Laboratories. *The Economic Effects of Fracture in the United States*. Number pt. 1 in NBS special publication. U.S. Department of Commerce, National Bureau of Standards, 1983.

[60] A. Rosolen, D. Millán, and M. Arroyo. Second order convex maximum entropy approximants with applications to high order pde. *International Journal for Numerical Methods in Engineering*, 94(2):150–182, 2013.

[61] I. V. Singh, B. K. Mishra, and M. Pant. An enrichment based new criterion for the simulation of multiple interacting cracks using element free galerkin method. *International Journal of Fracture*, 167(2):157–171, 2010.

[62] I.V. Singh, B.K. Mishra, and M. Pant. An efficient partial domain enriched {EFGM} criterion for the simulation of cracks in non-convex domains. *International Journal of Modeling Simulation and Scientific Computing*, 2:317 – 336, 2011.

[63] L.J. Sluys and R. de Borst. Dispersive properties of gradient-dependent and rate-dependent media. *Mechanics of Materials*, 18(2):131 – 149, 1994. Special Issue on Microstructure and Strain Localization in Geomaterials.

[64] T. Strouboulis, I. Babuška, and K. Copps. The design and analysis of the generalized finite element method. *Computer Methods in Applied Mechanics and Engineering*, 181(13):43 – 69, 2000.

[65] N. Sukumar. Construction of polygonal interpolants: a maximum entropy approach. *International Journal for Numerical Methods in Engineering*, 61(12):2159–2181, 2004.

[66] S. Wang and H. Zhang. Partition of unity-based thermomechanical meshfree method for two-dimensional crack problems. *Archive of Applied Mechanics*, 81(10):1351–1363, 2011.

[67] D.H. Winne and B.M. Wundt. application of the griffith-irwin theory of crack propagation to the bursting behavior of disks, including analytical and experimental studies. *Transactions of the American Society of Mechanical Engineers*, 80:1643–1655, 1958.